LBNL – 59266

TRACER GAS TRANSPORT UNDER MIXED CONVECTION CONDITIONS IN AN EXPERIMENTAL ATRIUM: COMPARISON BETWEEN EXPERIMENTS AND CFD PREDICTIONS

Buvaneswari Jayaraman, Elizabeth U. Finlayson, Michael D. Sohn,
Tracy L. Thatcher, Phillip N. Price, Emily E. Wood,
Richard G. Sextro, Ashok J. Gadgil

Environmental Energy Technologies Division
Indoor Environment Department
Lawrence Berkeley National Laboratory
One Cyclotron Road
Berkeley, California 94720

January 2006

This work was performed under the U.S. Department of Energy Contract No. DE-AC02-05CH11231.

TRACER GAS TRANSPORT UNDER MIXED CONVECTION CONDITIONS IN AN EXPERIMENTAL ATRIUM: COMPARISON BETWEEN EXPERIMENTS AND CFD PREDICTIONS

Buvaneswari Jayaraman*, Elizabeth U. Finlayson, Michael D. Sohn, Tracy L. Thatcher, Phillip N. Price, Emily E. Wood, Richard G. Sextro, Ashok J. Gadgil

Indoor Environment Department

Lawrence Berkeley National Laboratory

One Cyclotron Road, Mail Stop: 90R3058

Berkeley, California 94720, USA.

To be submitted to Atmospheric Environment

* Corresponding author: Tel: 510-486-6587

FAX: 510-486-6658

E-mail: bjayaraman@lbl.gov

Abstract

We compare computational fluid dynamics (CFD) predictions using a steady-state Reynolds Averaged Navier-Stokes (RANS) model with experimental data on airflow and pollutant dispersion under mixed-convection conditions in a 7 x 9 x 11m high experimental facility. The Rayleigh number, based on height, was $O(10^{11})$ and the atrium was mechanically ventilated. We released tracer gas in the atrium and measured the spatial distribution of concentrations; we then modeled the experiment using four different levels of modeling detail. The four computational models differ in the choice of temperature boundary conditions and the choice of turbulence model. Predictions from a low-Reynolds-number k-ε model with detailed boundary conditions agreed well with the data using three different model-measurement comparison metrics. Results from the same model with a single temperature prescribed for each wall also agreed well with the data. Predictions of a standard k-ε model were about the same as those of an isothermal model; neither performed well. Implications of the results for practical applications are discussed.

Keywords:

Mixed convection, indoor pollutant dispersion, turbulence model, atria

1. Introduction

Understanding the transient transport and dispersion of airborne pollution in large indoor spaces (such as atria, auditoria, airport lounges, and train stations) is of both scientific and practical interest. It is of scientific interest because it addresses an airflow and pollutant transport regime (turbulent mixed convection in enclosures) that has not been well characterized. It is of practical interest because understanding pollutant dispersion in large

indoor spaces is necessary to make exposure assessments, and to help develop responses to unexpected pollutant releases in such spaces.

Computational fluid dynamics (CFD) modeling has been used to predict airflow in large interior spaces in buildings, often as a tool for designing ventilation systems to provide thermal comfort and improve energy efficiency. Especially in the past few years, there has also been substantial interest in predicting pollutant transport in buildings that are believed to be potential targets for chemical or biological terrorism. Only a few researchers have investigated pollutant transport in large spaces, and those studies have been mostly limited to steady pollutant sources and sparse spatial sampling.

Shimada et al. (1996) and Murakami et al. (1988) studied transport of particles in small rooms by comparing model predictions to point measurements at a few sampling locations. Hiramatsu et al. (1996) carried out experiments and simulations of hourly time-integrated measurements of temperature and velocity in an experimental atrium of dimension 7 x 4.3 x 4.5 m. This study focused on understanding the thermal driving forces such as radiation, outdoor temperature, and infiltration in the space. Lee et al. (2002) investigated the effect of an inlet velocity distribution on indoor contaminant predictions in a 1 x 0.7 x 0.3 m high experimental chamber. They compared predictions from an isothermal analysis with data obtained at 117 locations and found that using the inlet velocity distribution to define inlet boundary conditions resulted in concentration estimates that were more reliable than predictions using a uniform velocity inlet boundary condition. See Gadgil et al. (2000) for an overview of research in this area.

These studies investigated airflow and pollutant dispersion in small rooms. Airflow in large, multi-storey indoor spaces such as auditoria, atria, and airport terminals is driven by a combination of forced convection due to HVAC equipment and natural convection due to heat sources and temperature differences between the surfaces. We refer to the combination of

natural and forced convection as mixed convection. Thermal effects are considered important when the square root of the Rayleigh number approaches or exceeds the Reynolds number. The Rayleigh number can be very high ($> 10^{10}$) for such tall spaces, leading to buoyancy-induced turbulence even in the absence of mechanical ventilation. For example, the conditions of the facility we study in this work result in a Rayleigh number of $2x10^{11}$.

The high-Reynolds-number k-ε model (standard k-ε model), which is widely used for indoor airflow applications, has been reported to perform poorly for natural- and mixed-convection flows (Chen et al. 1990, Moser 1991, Heiselberg et al. 1998). Chen et al. (1990) studied airflow in a room under natural convection with a Rayleigh number of 5×10^{10}. They found that the standard k-ε model under-predicted the heat transfer coefficient and recommended the use of a low-Reynolds-number turbulence model for computation of natural- and mixed-convection flows indoors.

Airflows in large spaces depend strongly on thermal effects. Unfortunately, thermal boundary conditions often are unknown or only poorly known for real-world (non-laboratory) conditions. The sparse data force modelers to assign temperatures and other boundary conditions based on engineering judgment. In tall rooms, where thermal effects are important, we expect that inaccuracies in the assigned temperatures could lead to errors in the predicted airflows. However, we know of no calculations or rules of thumb that quantify the level of detail in wall temperatures necessary to predict flows with a given level of accuracy. We do not provide such a calculation in this paper, but this research is a step in that direction.

Our goal in this paper is to gain insight into how the level of detail in the temperature boundary conditions and the choice of turbulence model affect the accuracy of the pollutant transport predictions. This issue is of substantial practical importance, because it helps to determine the appropriate level of effort for characterizing and modeling real-world large interior spaces. Specifically, we investigate the accuracy of steady-state k-ε Reynolds-

Averaged Navier-Stokes (RANS) CFD predictions using a low-Reynolds-number turbulence model with detailed prescription of temperature boundary conditions based on all of the available data. We then consider models incorporating less input information and simpler turbulence models. The general model characteristics are summarized in Table 1.

We compare model predictions to spatially distributed concentration measurements in the full size atrium described in Fischer et al. (2001). Path-integrated concentrations were measured along multiple short and long sampling paths in three horizontal planes every seven seconds. To our knowledge, CFD predictions of pollutant transport have not been compared to these types of spatially resolved data in the published literature.

2. Experimental setup

The experimental atrium shown in Figure 1 has dimensions 7 x 9 x 11m high (volume ~690 m^3). A dedicated heating and ventilation (HVAC) system supplies 590 L s^{-1} (1250 CFM) of air to the atrium at a temperature of 21^o C (70^o F) through a series of five wall-mounted supply registers that discharge horizontally into the atrium (Figure 1). The supply registers are 1.25 m wide and 0.3 m high. The exhaust outlet is located on the ceiling. For a complete description of the atrium, and of the typical experimental instrumentation can be found in Fischer et al. (2001).

Temperature sensors placed on the walls collected data at five-minute intervals. Each wall had 3 to 4 sensors arrayed approximately every 2 m vertically. There were 3 temperature sensors on the ceiling and one on the floor. The time-averaged temperatures during the experimental period are given in Table 2.

In the experiment, tracer gas comprising 4% methane in nitrogen was released continuously from a 1m^2 area source located 0.5 m above the floor at a flow rate of 0.5 L s^{-1} (1.06 CFM). The location of this source is indicated in Figure 1. The HVAC system was

operated to provide only outside air, i.e., there was no recirculation. The experiment was carried out for approximately 30 hours to obtain data over a variety of thermal conditions. Boundary temperatures were monitored but not controlled, so they varied with exterior conditions. Concentration measurements were based on infrared absorption by the methane tracer, with the nitrogen acting as a neutrally-buoyant diluent gas. Path-integrated concentrations were recorded every seven seconds along 27 short (0.5 m) and 30 long (2-10 m) paths at three heights, as shown in Figure 1. Figure 2 shows the arrangement of the short and long paths in the lowest measurement plane, at z = 2 m. This array is similar to measurement path arrangement at z = 4 m and z = 6 m. The lower two measurement planes are below the lowest air supply register (see Figure 1).

Figure 3a shows the time evolution of concentration along two short-paths in the lower measurement plane. For comparison to our steady-state CFD analysis, we chose a period (3:30-5:30 AM) during which the experimental airflows were fully-developed and the path-integrated concentrations stable. The vertical lines in Figure 3a show the bounds of the period over which the data were averaged. Figure 3b shows the close up view of the period of interest over which the data were averaged for comparison with CFD predictions.

3. CFD method

We obtained the steady-state airflow and temperature fields by solving the Reynolds Averaged Navier-Stokes equations (RANS) using the commercial CFD software, StarCD (Adapco 2004). The standard and low-Reynolds-number k-ε (Lien et al. 1996) models with buoyancy production terms were used to model the turbulence. The dilute methane tracer was treated as an active scalar; i.e., its presence influences the bulk physical properties of the background fluid. Physical properties such as density and molecular viscosity of the mixture (background fluid and tracer gas) were calculated by taking the weighted average of the

constituent properties. In work we reported earlier (Jayaraman et al. 2005) we also did simulations treating the tracer gas as a neutrally-buoyant scalar. We compare those results here.

The low-Reynolds-number model integrates the equations of turbulent kinetic energy and dissipation rate all the way to the wall, providing an alternative to the wall function approach used in the standard k-ε model. This requires a very fine mesh close to the wall, in order to resolve the laminar sublayer. The non-dimensional normal distance from the wall, y^+, in the near-wall cell should be of the order of 1. Previous studies (Chen et al. 1990, Murakami et al. 1996) have shown that the low-Reynolds-number model gives better heat transfer predictions near the walls and improved agreement with the data for natural- and mixed-convection flows.

The low-Reynolds-number turbulence model with hybrid wall functions was used in this study (Adapco 2004). The hybrid wall function uses a special wall boundary condition that allows a somewhat lower grid density in the near-wall region, resulting in a reduction of computational cost. If the mesh is fine enough, the boundary layer is resolved in a similar way as the low-Reynolds-number model. In regions of coarser mesh in the near-wall region adequate wall functions are applied using blending procedures (Adapco 2004).

For all but one case spatial discretization was carried out using the Monotone Advection and Reconstruction Scheme (MARS), a second-order scheme (Asproulis 1994) that suppresses numerical diffusion (See Table 1). The discrete finite volume system of equations was solved iteratively using the algebraic multigrid (AMG) method with a modified predictor-corrector SIMPLE algorithm and pseudo-transient time marching with a time step of 0.05 sec. We used a turbulent Schmidt number of 0.6. All computations were performed in parallel on a dual AMD Athlon 2200+ Linux cluster using 4 dual processor nodes.

3.1. Computational mesh

The computational mesh for simulations using the standard k-ε model consists of approximately 190,000 cells. In the core of the room, the grid cells have dimensions of 0.12 x 0.17 x 0.1m. The mesh is aligned with the flow direction near the supply registers in order to minimize numerical diffusion. Local mesh refinement was carried out normal to the walls for the simulations with the low-Reynolds-number turbulence model with hybrid wall functions. The refined mesh for simulations using the low-Re k-ε model has roughly 280,000 cells, resulting in a maximum y^+ of 9.8 near the wall.

3.2. Convergence criteria

The steady-state concentration field was obtained by solving the scalar mass transport equation in conjunction with mass, momentum and energy equations, along with the selected turbulence model. The calculations were considered converged when the cumulative normalized residual for all the flow variables dropped below 1×10^{-3} and the change in mass and energy balance in the domain fell below 1%.

3.3. Boundary conditions

In the experiment the HVAC-supplied air was approximately 2 ^{o}C hotter than the walls. The average surface temperature distribution is summarized in Table 2. The north, south and east wall are divided vertically into 4 segments and the west wall is divided vertically into 3 segments, such that each segment is centered on a temperature sensor. The temperature reported by the sensor in a given segment of wall is used to prescribe the temperature boundary condition for the entire segment (Table 2). The floor and the ceiling of the atrium have been assigned a uniform temperature boundary condition. The temperature of the tracer gas at the release location is estimated as 19 °C based on the measurements done after the experiments. The turbulence parameters at the HVAC inlet were 5% turbulence intensity and a length scale of 7% of the hydraulic diameter. The CFD simulation cases and temperature boundary conditions are presented in Tables 1 and 2.

The path-integrated concentration along the long and short-paths provided the basis for comparing the CFD simulations with experiment, as described below. Accurate prediction of concentrations requires accurate prediction of turbulent diffusion and flow velocities, since the tracer gas is transported by advection and diffusion. Qualitatively, we consider the CFD predictions to agree well with the data if the model and experimental results are within a factor of two (Finlayson et al. 2004). Quantitative comparison of CFD predictions is carried out based on three statistical metrics: R^2, Normalised Root Mean Square Error (NRMSE), and nearness factor.

4. Results and discussion

We carried out four CFD simulations of the experimental atrium (Table 1). The first simulation, Case A, used the most detailed thermal boundary conditions. The airflow and tracer gas concentrations are predicted using a low-Re turbulence model and MARS second-order differencing scheme.

The second simulation, Case B, used the same low-Re turbulence model and MARS scheme, but used simpler wall boundary conditions: each wall was assigned a uniform temperature equal to the average of the sensors on that wall.

The third simulation, Case C, used a standard k-ε turbulence model with the same thermal boundary condition as in Case B. The MARS second-order scheme led to convergence difficulties in this case so the simulation was carried out using a first-order upwind differencing scheme. In the standard k-ε model, wall functions relate the surface boundary conditions to the first grid point away from the wall and thus avoid modeling the viscous sub layer. But the universal wall functions are not suitable under conditions of low values of turbulent-Reynolds-number R_t that exist close to the wall. This leads to poor prediction of airflow near walls (Chen, 1990), resulting in deviation of the predictions in the

core flow. These models are nevertheless widely used in practice and we have an interest in seeing whether this approach can generate reasonably accurate results.

Finally, the fourth simulation, Case D, used a standard k-ε model but assumed isothermal conditions. This case serves as a baseline; this is the simplest CFD model one might employ, and modelers without access to data on thermal boundary conditions might be inclined to use such a model to obtain a rough guess as to airflows in the chamber.

Figures 4a and 4b show predicted velocities and temperatures in a vertical plane through the center of the air inlets from Case A. The air injected into the room is warmer than the air in the room, so Case A, like all of the non-isothermal CFD simulations, predicts that the inlet jets coalesce and rise towards the ceiling (Figure 4a). These simulations also show a stable stratification of temperature in the atrium (Figure 4b). The number of iterations and CPU times to obtain the solution are presented in Table 6.

We now investigate the performance of the four cases. We are interested in three general questions: (1) how well does the predicted concentration for each path agree with the measured path-average concentration; (2) how well does the predicted spatial pattern of high and low concentrations – i.e. the predicted three-dimensional map – agree with the measured spatial pattern of high and low concentrations; and (3) how well does the predicted spatial pattern of high and low concentrations within each measurement plane agree with the observations in that plane? These really are separate questions. For example, if the predicted concentrations everywhere were exactly half of the observed value, then the spatial patterns would match perfectly, but every prediction would be in error by a factor of two.

Qualitative discussion of model fit

Figure 5 compares a reconstruction of the experimental contours of tracer gas concentration in the lower measurement plane (z=2m) to the predictions from Case A. The

contours of the tracer gas for the experimental data are obtained using the tomographic reconstruction technique using both the short and long path data (Price et al. 2001). Visual comparison of Figures 5a and 5b shows that the simulated peak in the concentration compares well with that of the tomographic reconstruction. In addition, there is broad agreement between the predicted and observed West-to-East concentration gradient in the 2m plane. We will quantify this agreement in the next section.

Figures 6-9 show log-log plots of CFD predictions versus experimental measurements for Cases A-D respectively, for both the short-path and long-path measurements. For each data point, a horizontal bar indicates the range that contains the central 80% of the data; the resulting standard error of the measurement is much less than the size of the plotted data point in the case of the long-path measurements, and is approximately the size of the data point for the short-path measurements. Dashed diagonal lines delimit predictions that are too high or too low by a factor of two.

As the figures show, Cases A-C all correctly predict that concentrations in the lower and middle planes are much higher than in the upper plane. Case D performed very poorly in this regard because it assumes isothermal conditions whereas in fact the incoming air, which contained no tracer gas, was warm and thus buoyant; the result is that Case D greatly overestimates the amount of mixing in the lower plane.

For all of the cases the short-path measurements, which provide spatially resolved data, show that within any given plane there is poor correlation between predicted and observed concentrations. In general, the sensors that were predicted to have particularly high concentrations within a plane didn't actually have higher concentrations than those predicted to have low concentrations. The exceptions are (1) Case A correctly predicted the general spatial pattern in the lowest plane, and (2) all of the cases correctly predicted that the sensor

in the upper plane that is very close to an air inlet would have the lowest concentration in that plane.

The qualitative performance of the four models is as follows:

1. Case A, predicts concentrations that are biased high by a small amount for the lower plane. Most predictions agree with observations to within a factor of two everywhere in the chamber. The overall three-dimensional spatial pattern of high and low concentrations is fairly well reproduced, but the spatial pattern within each horizontal measurement plane is captured only in the lower plane.
2. Case B, predicts concentrations that are biased high by more than Case A, but still agree with the observations within a factor of 2 at most locations. The three-dimensional spatial pattern is fairly well reproduced, but the spatial pattern within each measurement plane is not captured, except partially in the lower plane.
3. Case C, predicts concentrations that are biased somewhat low in the uppermost plane and biased high by about a factor of two in the lower two planes. The three-dimensional spatial pattern of high and low concentration is reproduced fairly well but is exaggerated (i.e. regions of low concentration have predictions that are too low, and regions of high concentration have predictions that are too high). The spatial pattern within each measurement plane is not captured, except partially in the lower plane. These larger differences between the data and the predictions could be caused by the numerical diffusion due to the use of first-order upwind difference scheme for Case C.
4. Case D, predicts concentrations that are biased slightly high in the upper plane and biased very low in the lower two planes. The three-dimensional spatial pattern is very poorly reproduced: in contrast to reality, predicted concentrations in the lower planes are not much higher than in the upper plane. The spatial pattern within each measurement plane is not captured.

Quantitative discussion of model fit

To quantify the performance of the CFD models, we compare the CFD-predicted steady-state concentrations with the observed time-averaged concentrations. We use three measures of model fit, which are as follows.

Spatial correlation between the predictions and data within each plane is assessed by calculating R^2. R^2 values close to 1 indicate very good correlation, and close to zero indicate poor correlation. We calculated R^2 in both untransformed space and from a fit of log(predicted concentration) versus log(observed concentration); the log-space values are arguably preferable because they are based on relative rather than absolute errors, and because the experimental uncertainties in the measured mean concentrations increase with concentration.

The absolute agreement between experiments and simulations is summarized by root-mean-square error of the logs (RMSEL):

$$\text{RMSEL}=\sqrt{\frac{1}{N}\sum_{i=1}^{N}(\log(C_i)-\log(\hat{C}_i))^2} \qquad (1)$$

where C_i is a measured concentration and $\hat{C}_i$ is the corresponding predicted concentration. We present the exponential of RMSEL in Tables 3,4. An Exp(RMSEL) value of 1 indicates that the predictions are in perfect agreement with the data and a value of 2 indicates that the predictions are about twice the data.

"Nearness", is a measure used by some researchers to determine the quality of the predictions (Herman et al. 1973). Nearness quantifies the error in predicted concentration normalized to the standard deviation of the concentrations:

$$\text{Nearness} = \sqrt{\frac{\sum_i \left(C_i - \hat{C}_i\right)^2}{\sum_i \left(C_i - \overline{C}\right)^2}} \qquad (2)$$

where $\overline{C}$ is the mean of the measured concentrations. Nearness values close to zero indicate good agreement between data and predictions. Nearness = 0.5 means that the RMS error is half the RMS variation in concentration measurements.

Each of the measures of model fit quantifies a different type of discrepancy between predictions and measurements. R^2 quantifies the extent to which sensors that are predicted to have higher- or lower-than-average concentrations actually do so, but does not quantify the absolute error: R^2 would be high if all of the predictions were in error by the same large factor, for example. In contrast, RMSEL and Nearness quantify the magnitude of the error in the predictions, but not whether high (or low) predictions are associated with high (or low) observations, and thus, for the spatial data discussed here, whether the spatial pattern of the predictions is captured correctly.

Table 3a shows the measures of model fit when applied to short-path sensor data from the entire chamber. Cases A, B, and C all have comparable (and rather high) values of R^2 in both untransformed and log space. These high values show these models correctly predict that the lower plane has high concentrations, while the upper and middle plane have low concentrations that are comparable to each other. In contrast, the low R^2 for Case D occurs because this model performed very poorly from the standpoint of predicting which parts of the chamber have higher- or lower-than-average concentrations: concentrations in the lower plane were erroneously predicted to be about as high as in the upper and middle plane. The measures of the model fit for the long-paths are shown in Table 3b.

Predictions from Case A have the lowest RMSEL's: errors are about 0.5 times the mean concentration. Case C had substantially larger RMSEL (and worse "Nearness") than

Case A because it suffers from substantial bias. While Case C correctly predicts the relative relationship between the concentrations in the various planes, its concentration predictions for the upper plane are too low, and for the lower planes the predictions are too high.

Table 4a,b summarizes the measures of model fit for the short and long-path data within each horizontal measurement plane. Case A does well at predicting the spatial distribution of gas in the plane closest to the gas release (i.e. the lower plane where the effects of mechanical mixing are smallest), and thus predicting which sensors report high, medium, and low concentrations. Therefore it achieves a high R^2 in the lower plane. Cases B and C perform somewhat less well in this regard, and Case D (the isothermal case) shows no correlation between predictions and measurements in the lower plane. None of the cases predict the spatial distribution in the middle or upper planes. Case D achieves a moderate R^2 in the middle plane for the short and long-paths, but predicts the spatial pattern in that plane completely incorrectly. For the short-paths it predicts high-concentration sensors to be low, and vice versa, and the correlation between predictions and measurements is negative.

Case A performs best in terms of the RMSEL as well: errors are about 30% of the mean concentration in the lower plane, about 60% of the average concentration in the middle plane and 1.6 times the average concentration in the upper plane. However, as the Nearness parameter indicates, the magnitude of the errors is about 1.2 to 2 times larger than the magnitude of the observed variability within the plane. Cases B and C predict the spatial distribution in the lower plane somewhat worse than does Case A, as evidenced by their lower values of R^2, and (like Case A) they fail to predict the spatial distribution within the middle and upper planes.

The histograms of the ratio of observations to predictions (Fig. 10) summarize the performance of the different models in predicting the tracer gas concentrations along the short and long paths. The x-axis represents the intervals (bins) and the y-axis shows the number of

paths in each interval, so if one ignores the plotting symbols the result is a conventional histogram. Additionally, the point representing each path is labeled by L (lower), M (middle), or U (upper), corresponding to the plane containing the path. We can see from Figure 10 that the tracer gas concentrations predicted by Case A and Case B using the low-Reynolds-number turbulence model are in good agreement with the data.

Neutrally-buoyant scalar simulations

We also carried out simulations by treating the tracer gas as a neutrally-buoyant scalar (Jayaraman et al. 2005). The advantage of treating the tracer gas as neutrally-buoyant is that the calculations require much less CPU time (Table 6). In this case we first solved the steady-state airflow. Using the airflow as background, we then solved the tracer gas transport equation. The model assumes that the tracer gas has the same physical properties as air. Table 5a,b summarizes the measures of model fit for the short and long-path data. The RMSEL and Nearness metrics show that this assumption leads to larger differences between the predictions and data compared to the results presented here. Even though Case A shows somewhat better correlation for the short-path data in all three planes, the accuracy of the prediction is lost in the lower plane compared to the result presented here. These larger differences are due to neglecting the density difference between the tracer gas and the background air.

5. Conclusion

This study reports a comparison between detailed, high quality measurements of tracer gas dispersion in an atrium under mixed convection conditions and the corresponding predictions from CFD models. Comparison of such spatially and temporally highly resolved data and predictions is carried out for the first time for an actual size atrium.

The steady-state airflow and concentration predictions obtained using a low-Re turbulence model with the MARS second-order scheme resulted in the best agreement with the experimental data, both in the chamber as a whole and within the lowest measurement plane. Further investigation is required to improve the predictions in the middle and upper plane. As expected, prescribing non-uniform temperature boundary conditions based on all the available temperature data resulted in better agreement between CFD predictions and measurements than did assigning a uniform temperature to each wall.

Also as expected, the standard k-ε model with first-order upwind difference scheme led to predictions substantially worse than those from the low-Re model. However, for many purposes these predictions would be acceptable, since they do predict the average concentration in all three measurement planes to within a factor of two or so, and they correctly predict that the upper plane has concentrations about equal to those in the middle plane, and much lower than the concentrations in the lower plane.

Unsurprisingly, the isothermal CFD model performed very poorly in predicting the spatial distribution of tracer gas; indeed, due to ignoring thermal buoyancy and stratification it erroneously predicts concentrations in the upper plane to be as high as concentrations in the lower and middle planes.

Our simulations show that the level of complexity of the model can be selected based on the kind of questions that need to be answered with the simulations. The average behavior of the tracer gas can be predicted using simple and faster models such as neutrally-buoyant tracer models, but the resulting predictions of pollutant dispersion can be less accurate. When higher accuracy predictions of tracer gas concentration are needed to address questions regarding sensor placement, exposure etc. a more accurate model should be used.

In the present study the flow is stably stratified in the atrium. Further research is required to understand the applicability of the current observations for unstably stratified flows and to improve the spatial correlation between data and predictions.

Acknowledgements

The authors would like to thank Douglas Black for his help with the measurements in the experimental atrium, David Lorenzetti and Mark Sippola for their editorial comments, John Rogers and Scott Wilensky of CD-adapco for their help with STAR-CD, and Rose McClellan and Kambiz Salari of Lawrence Livermore National Laboratory for helpful suggestions. This work was performed under the U.S. Department of Energy Contract No. DE-AC02-05CH11231.

References

Adapco 2004. "StarCD Version 3.20: Methodology," CD adapco group.

Asproulis, P. N., 1994. High resolution numerical predictions of hypersonic flows on unstructured meshes. Ph.D Dissertation, Imperial College, Dept. of Aeronautics, London, England.

Chen, Q., Moser, A., and Huber, A., 1990. Prediction of buoyant, turbulent flow by a low-Reynolds-number k-ε model. ASHRAE Transactions 96(1): 564-573.

Finlayson, E. U., Gadgil, A. J., Thatcher, T. L., and Sextro, R. G., 2004. Pollutant dispersion in a large indoor space: Computational Fluid Dynamics (CFD) predictions and comparisons with a scale model experiment for isothermal flow. Indoor Air 14(4): 272-283.

Fischer, M. L., Price, P. N., Thatcher, T. L., Schwalbe, A. S., Craig, M. J., Wood, E. E., Sextro, R. G., and Gadgil, A. G., 2001. Rapid measurement and mapping of tracer gas concentrations in a large indoor space. Atmospheric Environment 35: 2837-2844.

Gadgil, A. J., Finlayson, E. U., Fischer, M. L., Price, P. N., Thatcher, T. L., Craig, M. J., Hong, K. H., Housman, J., Schwalbe, C. A., Wilson, D., Wood, E. E., and Sextro, R. G., 2000. Pollutant transport and dispersion in large indoor spaces: A status report for the large space effort of the interiors project, LBNL-44791.

Heiselberg, P., Murakami, S., and Roulet, C. A., 1998. Ventilation of large spaces in buildings: Analysis and prediction techniques. IEA Annex 26: Energy efficient ventilation of large enclosures.

Herman, G.T., Lent A., and Rowland S.W., 1973. ART: Mathematics and Applications. A report on the mathematical foundations and on the applicability to real data of the algebraic reconstruction techniques. J. Theoretical Biology 42: 1-32.

Hiramatsu, T., Harada, T., Kato, S., Murakami, S., and Yoshino, H., 1996. Study of thermal environment in experimental real-scale atrium, 5th International conference on Air Distribution in Rooms, ROOMVENT'96, Yokohoma, Japan July 17-19, pp.523-530.

Jayaraman, B., Finlayson, E. U., Wood, E. E., Thatcher, T. L., Sohn, M. D., Price, P. N., Sextro, R. G., and Gadgil, A. J., 2005. Comparison between experiments and CFD predictions of mixed convection flows in an atrium, Indoor Air 2005, Sep 4-9, 2005, Beijing, China. LBNL-57100.

Lee, E., Feigley, E. C., and Khan, J., 2002. An investigation of air inlet velocity in simulating the dispersion of indoor contaminants via computational fluid dynamics. Ann. Occupational Hygiene 46(8): 701-712.

Lien, F. S., Chen, W. L., and Leschziner, M, A., 1996. Low-Reynolds-number-eddy-viscosity modeling based on non-linear stress-strain/vorticity relations. Proc. 3rd Symp. On Engineering Turbulence Modeling and Measurements, Crete, Greece.

Moser, A., 1991. The message of Annex 20: Airflow patterns within buildings. Proc. 12th AIVC conference, Air Movement and Ventilation Control within Buildings.

Murakami, S., Kato, S., and Suyama, Y., 1988. Numerical and experimental study on turbulent diffusion fields in conventional flow type clean rooms. ASHRAE Transactions 94: 469-493.

Murakami, S., Kato, S., Chikamoto, T., Laurance, D. and Blay, D., 1996. New low-Reynolds-number k-ε model including damping effect due to buoyancy in a stratified flow field. Int. J. Heat Mass Transfer 39(16): 3483-3496.

Price, P. N., Fischer, M. L., Gadgil, A. J., and Sextro, R. G., 2001. An algorithm for real-time tomography of gas concentrations using prior information about spatial derivatives. Atmospheric Environment 35: 2827-2835.

Shimada, M., Okuyarna, K., Okazaki, S., Asai, T., Matsukura, M. and Ishizu, Y., 1996. Numerical simulation and experiment on the transport of fine particles in a ventilated room. Aerosol Science and Technology 25: 242-255.

Figure 1: *3-D view of the experimental atrium showing locations of air supply and exhaust vents, tracer gas release location, and tracer gas measurement heights.*

Figure 2: *Plan view of the optical path geometry for the measurement plane at z=2m above the floor. Thin lines indicate ray paths of the 10 long-path sensors. A first-surface mirror at the vertex of each path reflects the infrared ray to the detector. (The thick lines indicate ray paths of the 9 short-path sensors)*

Figure 3. *Concentration data along two short-paths in the lower plane. The vertical solid lines indicate the period over which the data were averaged for comparison with CFD predictions.(a). Concentration data for the entire duration of the experiment.(b). Close up view of the period over which the data were averaged.*

Figure 4. *Predictions based on simulation Case A: (a) Velocity field in a vertical plane perpendicular to the air supply inlets, with the inlets at the right edge of the figure. (b) Temperature contours in a West-to East vertical plane through the source.*

Figure 5. *Tracer gas concentration contours in the lower (z=2m) plane.(a) Tomographically reconstructed experimental data. (b) CFD predictions based on Case A.*

Figure 6: *Comparison of path-averaged concentrations measured experimentally and predicted with CFD along (a) short and (b) long paths, for non-uniform temperatures for walls and low-Re turbulence model (see Case A, Table 1 for details). Horizontal lines indicate the central 80% interqunatile range of the data.*

Figure 7: *Comparison of path-averaged concentrations measured experimentally and predicted with CFD along (a) short and (b) long paths, for walls with different uniform temperatures and low-Re turbulence model (see Case B, Table 1 for details).*

Figure 8: *Comparison of path-averaged concentrations measured experimentally and predicted with CFD along (a) short and (b) long paths, for walls with different uniform temperatures and standard k-ε turbulence model (see Case C, Table 1 for details).*

Figure 9: *Comparison of path-averaged concentrations measured experimentally and predicted with CFD along (a) short and (b) long paths, for isothermal walls (see Case D, Table 1 for details).*

Figure 10: *Histograms of the ratio of observations to predictions along the short and long paths for cases A-D for simulations treating the tracer gas as an active scalar.*

Table 1: *Simulation cases.*

Case	Turbulence model	Temperature and wall boundary conditions	Discretization scheme
A	Low-Re	Non-isothermal; segments of the four walls assigned temperatures according to the sparse measurements (See Table 2)	MARS
B	Low-Re	Non-isothermal; each wall at uniform temperature	MARS
C	Standard k-ε	Non-isothermal; each wall at uniform temperature	First order upwind
D	Standard k-ε	Isothermal; all walls (and air) at the same temperature	MARS

Table 2: *Average surface temperatures as a function of vertical location.*

Wall	**Uniform T ^{o}C**	**Non-uniform T ^{o}C**			
		Segment 1	**Segment 2**	**Segment 3**	**Segment 4**
South	18.9	19.2	17.9	20.0	18.6
	$0 \le z \le 11$	$0 \le z \le 2$	$2 < z \le 4.1$	$4.1 < z \le 6.8$	$6.8 < z \le 11$
North	19.2	19.7	19.9	19.3	18.0
	$0 \le z \le 11$	$0 \le z \le 2$	$2 < z \le 4.1$	$4.1 < z \le 6.8$	$6.8 < z \le 11$
West	17.2	17.4	15.7	18.5	N/A
	$0 \le z \le 11$	$0 \le z \le 3$	$3 < z \le 7.6$	$7.6 < z \le 11$	-
East	18.5	17.9	19.5	18.2	18.3
	$0 \le z \le 11$	$0 \le z \le 2$	$2 < z \le 4.1$	$4.1 < z \le 6.8$	$6.8 < z \le 11$
Floor	19.8	N/A	N/A	N/A	N/A
Ceiling	18.2	N/A	N/A	N/A	N/A

Table 3a: *Comparison of CFD predictions and data for the entire facility, for the short measurement paths.*

Case	R^2	R^2 in log space	Exp(RMSEL)	Nearness
A	0.6	0.8	1.5	0.9
B	0.5	0.8	1.7	1.3
C	0.7	0.9	2.1	2.3
D	0.0	0.1	2.0	1.2

Table 3b: *Comparison of CFD predictions and data for the entire facility, for the long measurement paths.*

Case	R^2	R^2 in log space	Exp(RMSEL)	Nearness
A	0.7	0.8	1.4	0.6
B	0.7	0.9	1.3	0.6
C	0.9	0.9	1.7	1.5
D	0.1	0.2	2.2	1.3

Table 4a: *Comparison of CFD predictions and data within each measurement plane, for the short measurement paths for an active scalar. * Indicates that R is negative.*

Case	R^2			R^2 in log space			Exp(RMSEL)			Nearness		
	Lower Z=2m	Middle Z=4m	Upper Z=6m	L	M	U	L	M	U	L	M	U
A	0.8	0.0	0.1	0.7	0.0	0.2	1.3	1.7	1.6	1.2	1.6	2.1
B	0.4	0.0	0.3	0.3	0.0	0.4	1.5	1.9	1.5	1.7	2.3	1.5
C	0.5	0.2	0.1	0.4	0.2	0.2	2.3	2.4	1.8	4.1	3.5	1.6
D	0.1	*0.4	0.0	0.2	*0.4	0.0	2.1	2.3	1.6	2.1	1.8	2.1

Table 4b: *Comparison of CFD predictions and data within each measurement plane, for the long measurement paths for an active scalar.*

Case	R^2			R^2 in log space			Exp(RMSEL)			Nearness		
	Lower Z=2m	Middle Z=4m	Upper Z=6m	L	M	U	L	M	U	L	M	U
A	0.6	0.0	0.0	0.6	0.0	0.0	1.2	1.4	1.5	1.0	1.6	3.7
B	0.2	0.0	0.0	0.2	0.0	0.0	1.2	1.4	1.3	1.1	1.8	2.0
C	0.5	0.0	0.4	0.5	0.0	0.4	1.7	1.6	1.7	3.9	3.6	2.9
D	0.4	0.3	0.2	0.4	0.2	0.2	2.4	2.6	1.4	3.3	3.2	3.0

Table 5a: *Comparison of CFD predictions and data within each measurement plane, for the short measurement paths for a neutrally-buoyant scalar. * Indicates that R is negative.*

Case	R^2			R^2 in log space			Exp(RMSEL)			Nearness		
	Lower Z=2m	Middle Z=4m	Upper Z=6m	L	M	U	L	M	U	L	M	U
A	0.8	0.2	0.5	0.6	0.1	0.5	1.8	1.5	1.7	4.2	1.2	2.4
B	0.6	0.0	0.1	0.6	0.0	0.1	1.3	2.1	2.0	1.3	3.3	3.7
C	0.0	0.2	0.3	0.0	0.2	0.4	10.	2.7	1.3	32.	5.0	0.9
D	*0.2	*0.5	0.2	*0.3	*0.5	0.3	2.2	2.4	1.4	2.1	1.9	1.4

Table 5b: *Comparison of CFD predictions and data within each measurement plane, for the long measurement paths for a neutrally-buoyant scalar.*

Case	R^2			R^2 in log space			Exp(RMSEL)			Nearness		
	Lower Z=2m	Middle Z=4m	Upper Z=6m	L	M	U	L	M	U	L	M	U
A	0.4	0.1	0.0	0.5	0.1	0.0	1.4	1.3	1.6	2.9	1.4	4.3
B	0.4	0.0	0.0	0.4	0.0	0.0	1.3	1.6	1.6	1.6	3.0	4.6
C	0.4	0.2	0.2	0.4	0.2	0.2	7.8	1.8	1.3	36	4.3	1.8
D	0.5	0.4	0.1	0.4	0.3	0.1	2.5	2.7	1.4	3.4	3.4	2.4

Table 6: *Computational details.*

Case	**Active Scalar**		**Neutrally-Buoyant Scalar**		
	Iterations	**CPU (Hours)**	**Iterations**		**CPU (Hours)**
			Airflow	**Scalar**	
A	15376	19	6987	10232	9
B	37653	52	10498	9588	11.5
C	67725	58	27890	7792	22
D	3791	3	157	13208	3.05

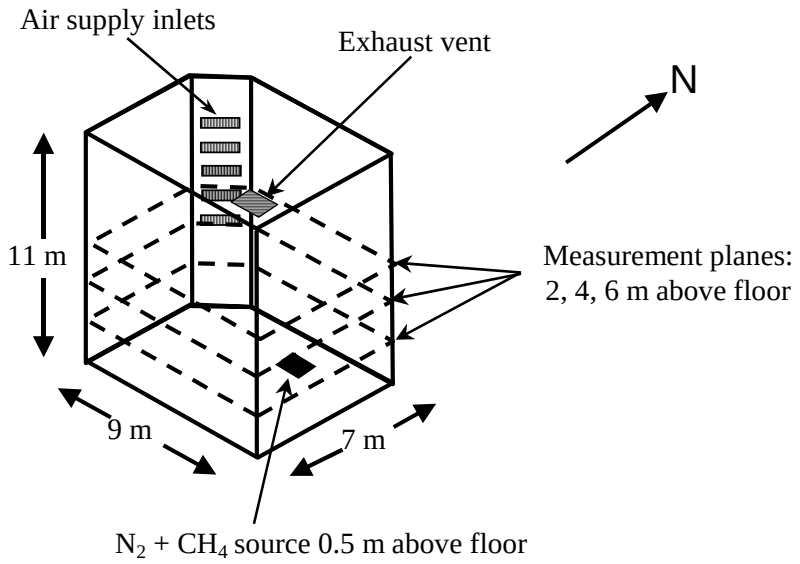

Figure 1: *3-D view of the experimental atrium showing locations of air supply and exhaust vents, tracer gas release location, and tracer gas measurement heights.*

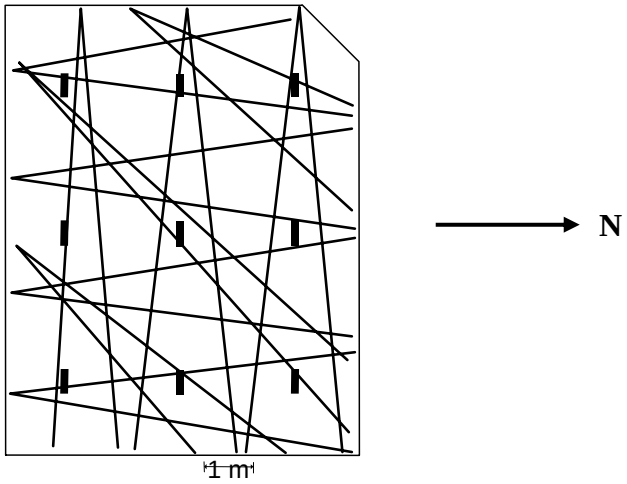

Figure 2: *Plan view of the optical path geometry for the measurement plane at z=2m above the floor. Thin lines indicate ray paths of the 10 long-path sensors. A first-surface mirror at the vertex of each path reflects the infrared ray to the detector. (The thick lines indicate ray paths of the 9 short-path sensors)*

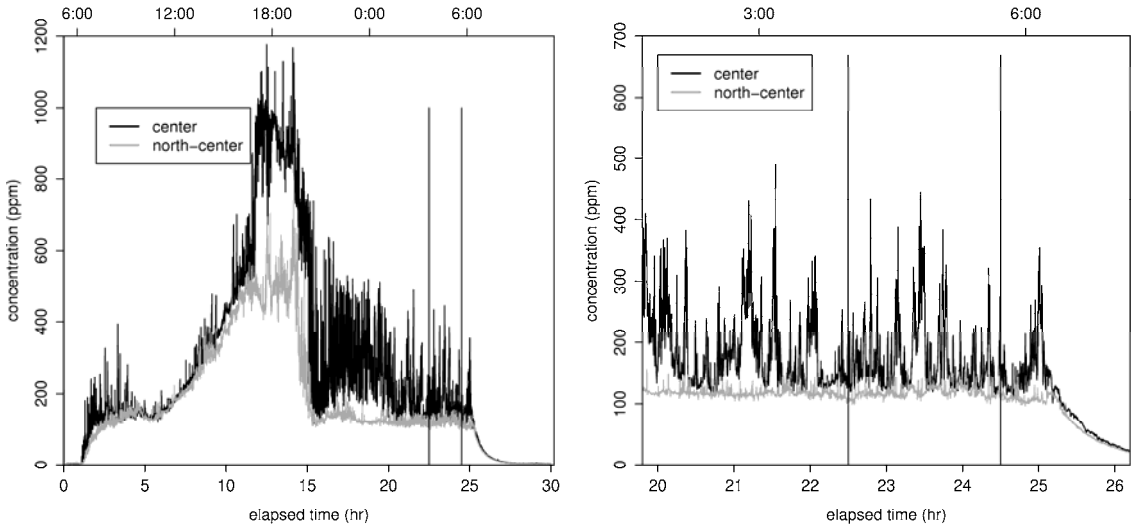

(a) *(b)*

Figure 3. *Concentration data along two short-paths in the lower plane. The vertical solid lines indicate the period over which the data were averaged for comparison with CFD predictions.*

(a). Concentration data for the entire duration of the experiment.

(b). Close up view of the period over which the data were averaged.

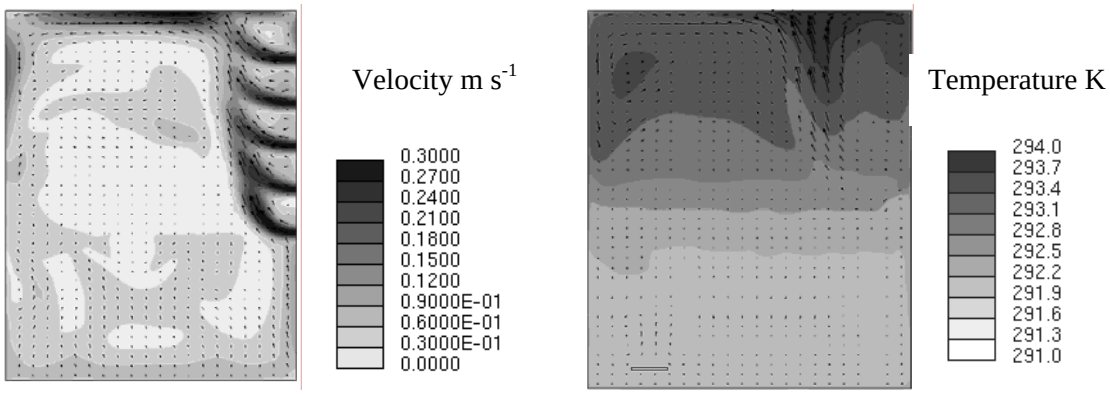

(a) *(b)*

Figure 4. *Predictions based on simulation Case A:*

(a) Velocity field in a vertical plane perpendicular to the air supply inlets, with the inlets at the right edge of the figure.

(b) Temperature contours in a West-to East vertical plane through the source.

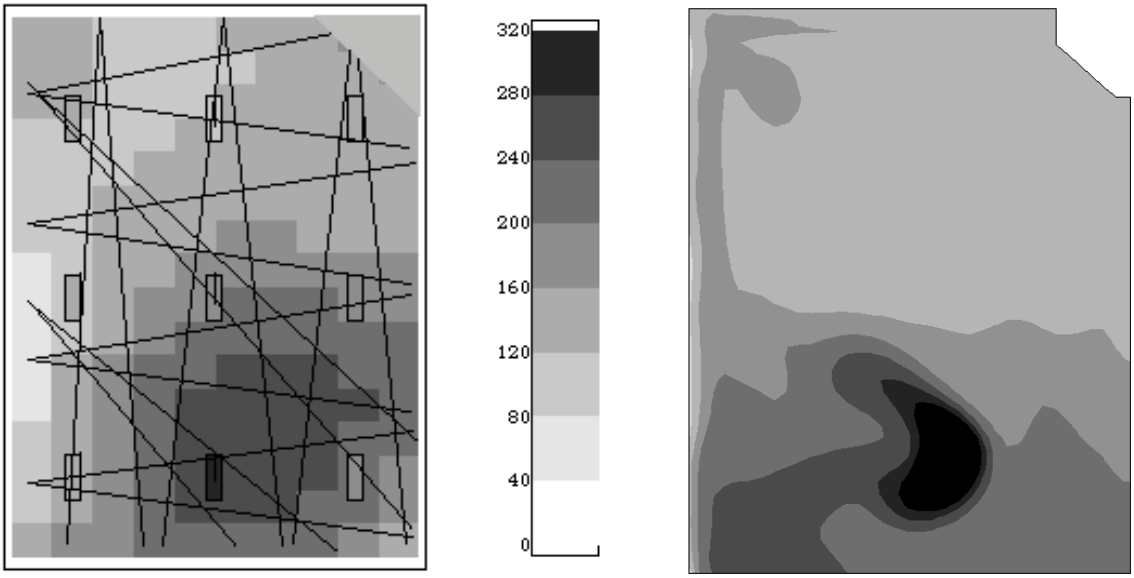

(a) *(b)*

Figure 5. *Tracer gas concentration contours in the lower (z=2m) plane.*

(a) Tomographically reconstructed experimental data.

(b) CFD predictions based on Case A.

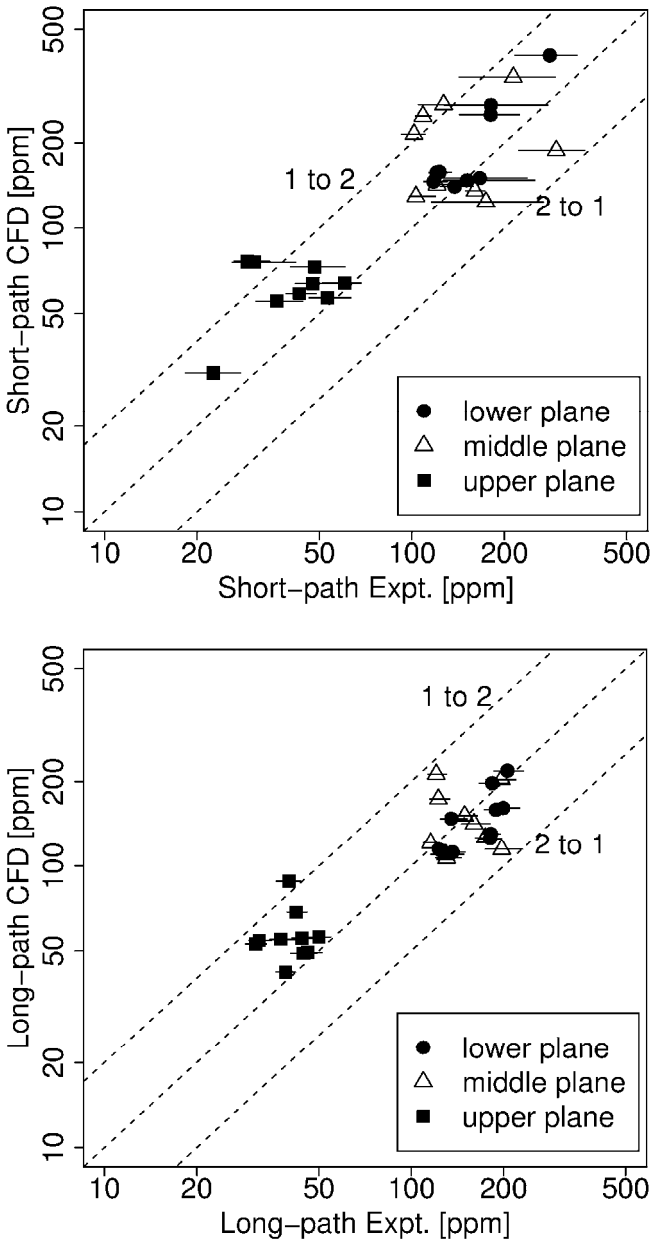

Figure 6: *Comparison of path-averaged concentrations measured experimentally and predicted with CFD along (a) short and (b) long paths, for non-uniform temperatures for walls and low-Re turbulence model (see Case A, Table 1 for details). Horizontal lines indicate the central 80% interquantile range of the data.*

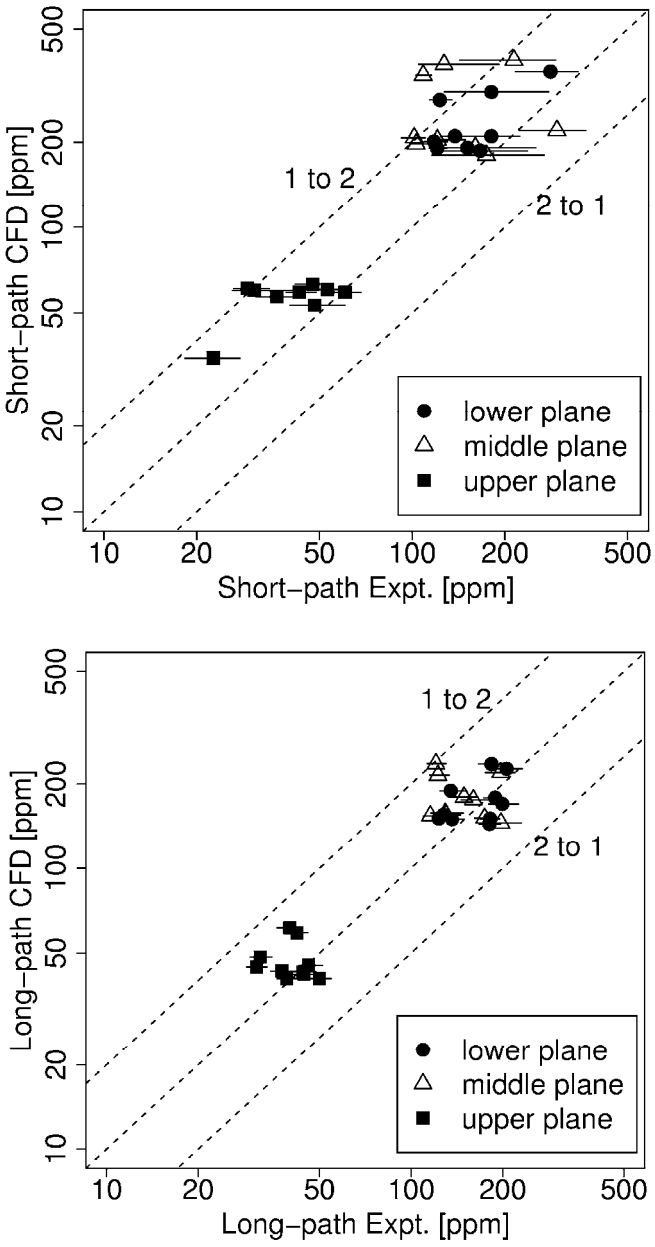

Figure 7: *Comparison of path-averaged concentrations measured experimentally and predicted with CFD along (a) short and (b) long paths, for walls with different uniform temperatures and low-Re turbulence model (see Case B, Table 1 for details).*

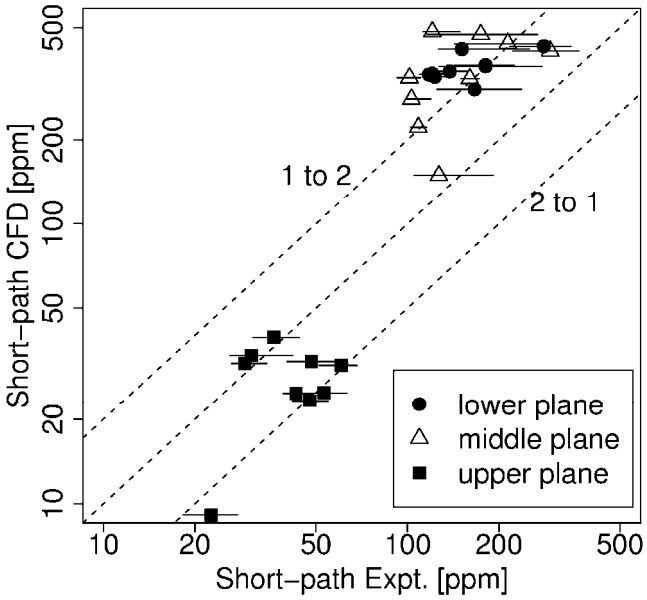

(a)

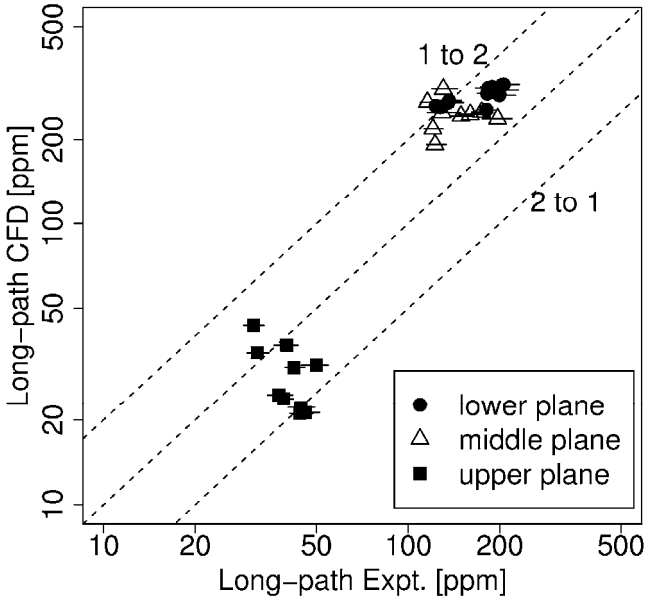

(b)

Figure 8: *Comparison of path-averaged concentrations measured experimentally and predicted with CFD along (a) short and (b) long paths, for walls with different uniform temperatures and standard k-ε turbulence model (see Case C, Table 1 for details).*

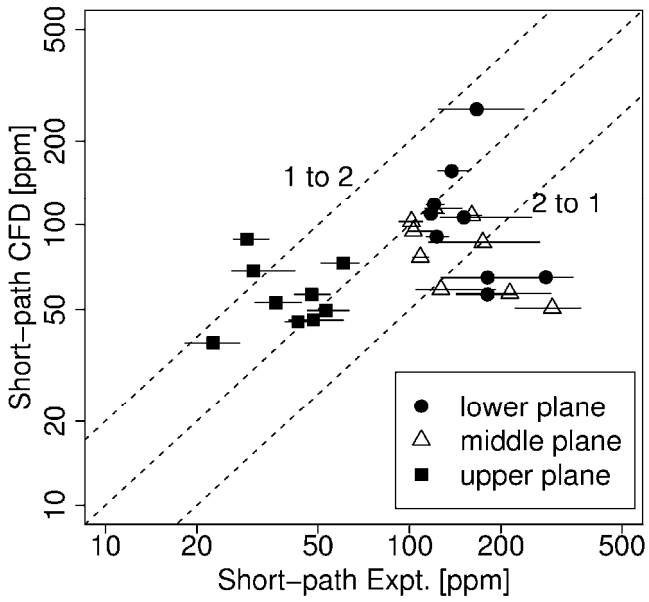

(a)

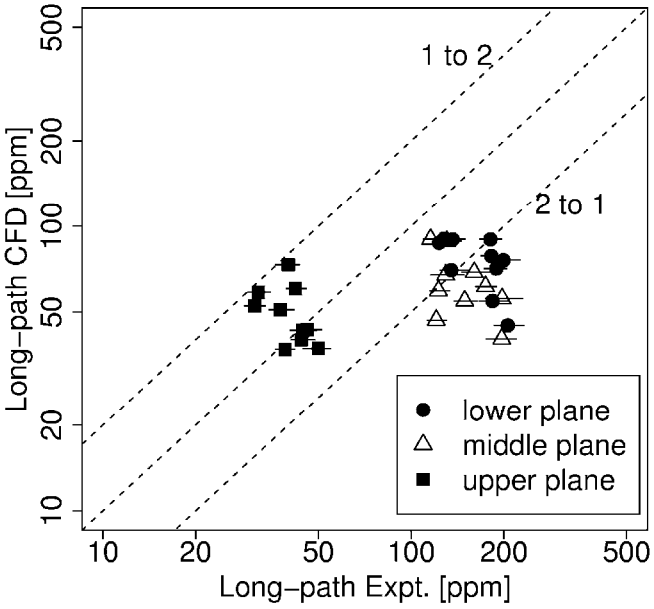

(b)

Figure 9: *Comparison of path-averaged concentrations measured experimentally and predicted with CFD along (a) short and (b) long paths, for isothermal walls (see Case D, Table 1 for details).*

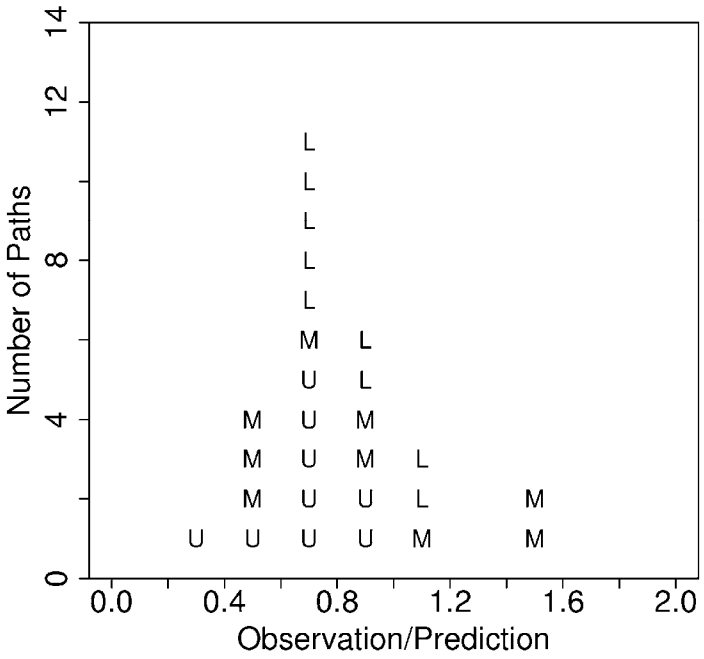

Case A:
Short Path

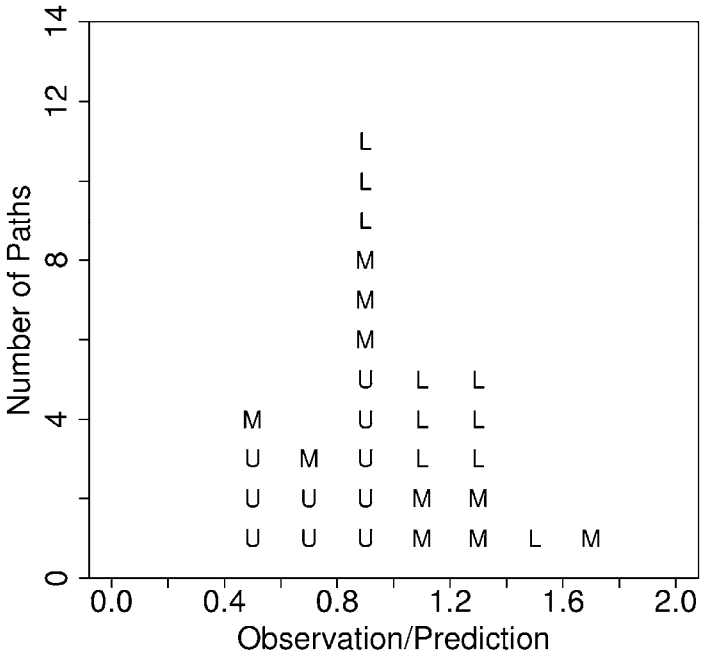

Case A:
Long Path

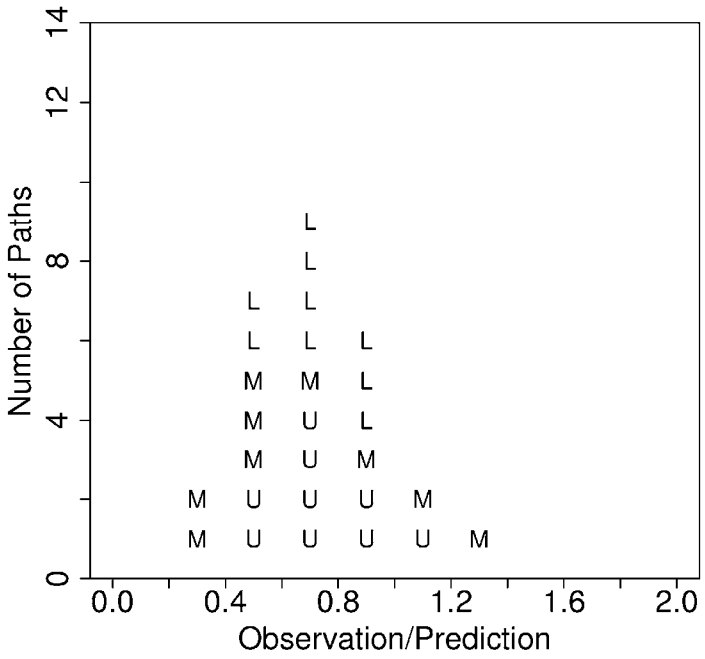

Case B:
Short Path

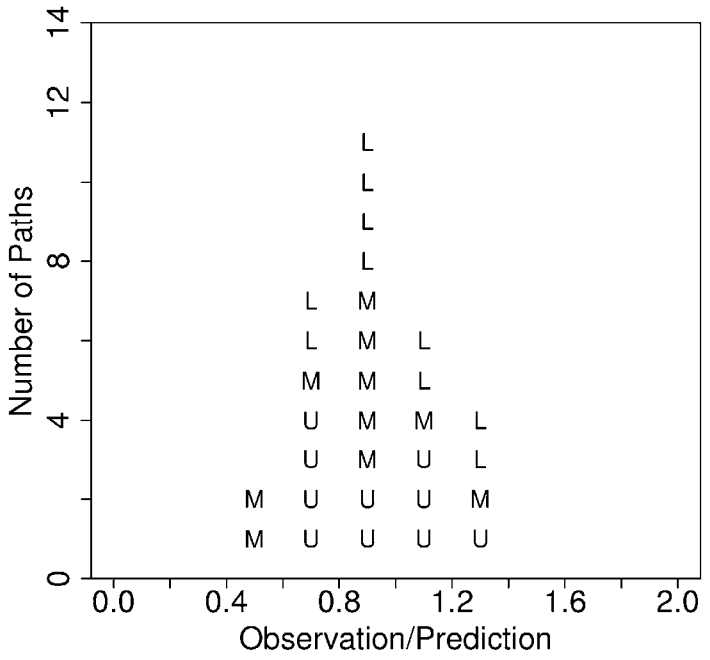

Case B:
Long Path

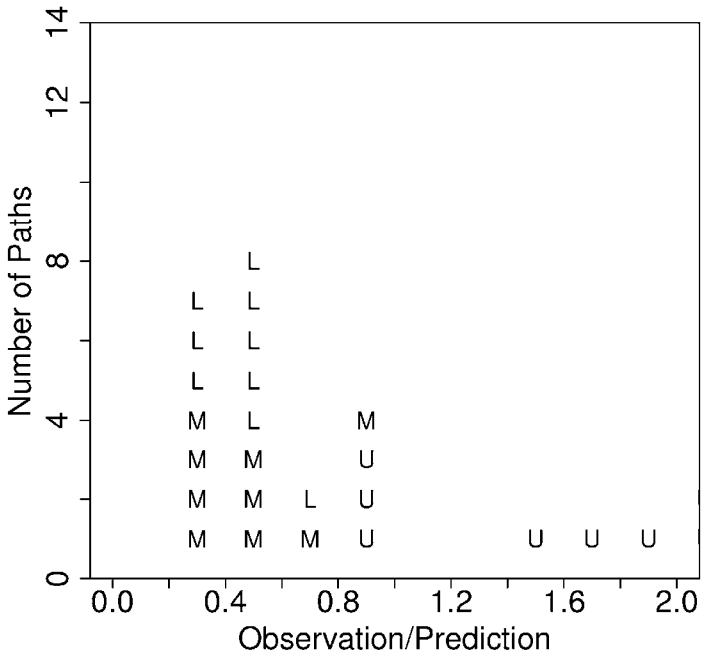

Case C:
Short Path

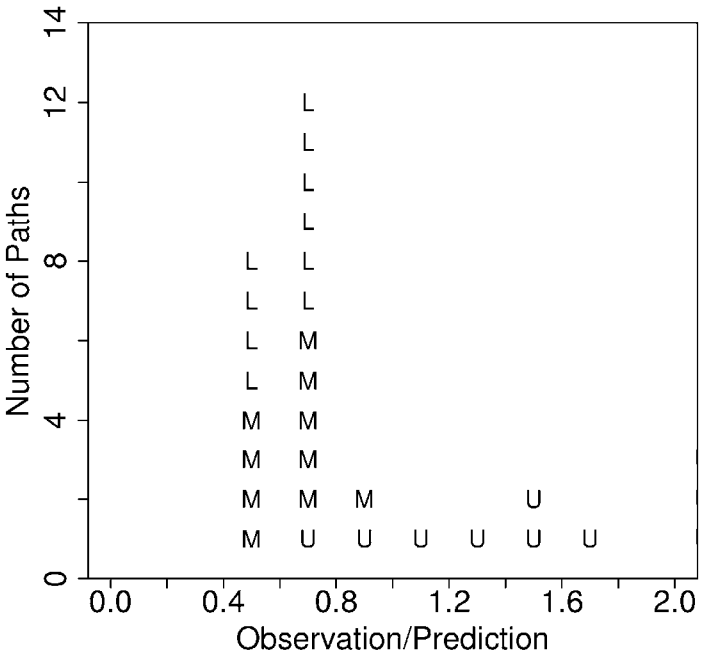

Case C:
Long Path

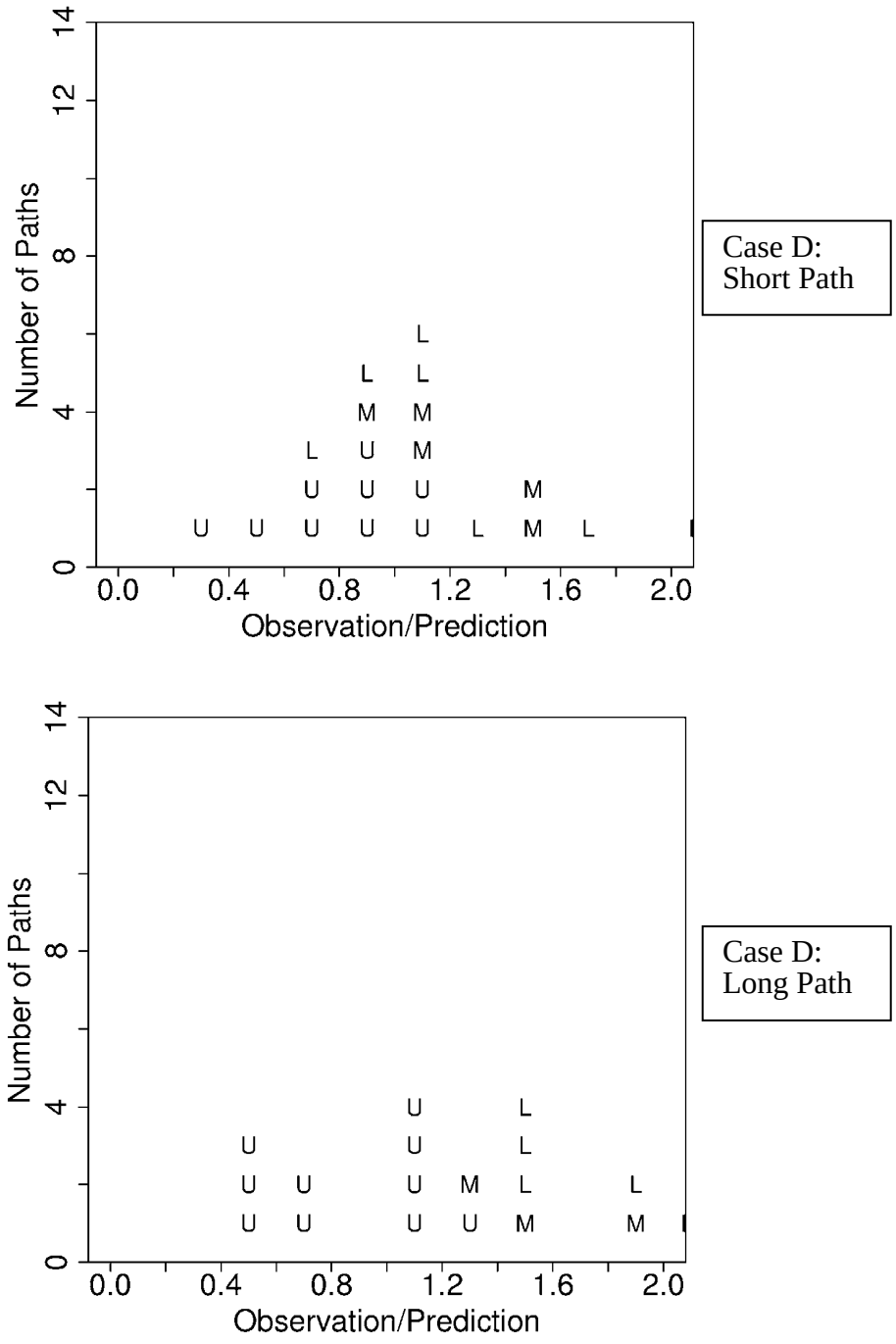

L-Lower, M-Middle and U-Upper plane

Figure 10: *Histograms of the ratio of observations to predictions along the short and long paths for cases A-D for simulations treating the tracer gas as active scalar.*